

Swarm Robotics in the Realm of Active Matter

Rapport comité de suivi 2022

Jérémy FERSULA

INSTITUT DES SYSTÈMES INTELLIGENTS ET DE ROBOTIQUE UMR 7222
LABORATOIRE GULLIVER UMR 7083
SORBONNE UNIVERSITÉ

Supervisors :

Nicolas BREDECHE
Olivier DAUCHOT
Marco TARZIA

Sorbonne Université
Institut des Systèmes Intelligents et de Robotique UMR 7222
Laboratoire Gulliver UMR 7083
Paris, France
January 2023

Introduction

This progress report describes a major part of the work done in the framework of the PhD entitled "Swarm Robotics : distributed e-learning in the field of Active Matter". Although incomplete, the main achievements are presented : experimental setup, preliminary data, theoretical study on individual robot dynamics. Not presented in this report (or very briefly) is the experimental setup in place since December 2021 and the processing of experimental data that corroborate the equations describing the individual dynamics of robots.

1. Experimental Setup

1.1 The Kilobot

1.1.1 Original Robot. Kilobots are low cost robots designed at Harvard University's Self-Organizing Systems Research Lab in the early 2010's, which began to get traction in the swarm robotics community along with a 2014 article (1) proposing a self-assembly algorithm experimentally tested on a Kilobot swarm of a thousand robots. The robot is designed to perform tasks in swarms of hundreds of individuals, that is, the bare robot is as simple as possible but complex tasks can be achieved by large scale coordination. The Kilobot is equipped with an ATMega 8bit @ 8MHz processor as well as 32KB Flash memory, to which programs can be uploaded via Infrared using the Over-Head Controller (OHC), another piece of hardware built as an interface from the computer to the Kilobot.

One Kilobot is 33mm wide, 34mm tall and equipped with an on-board close range infrared emitter/receiver, placed on the bottom of the circuit board. On top of the board are placed a light intensity sensor, a RGB led, two motors and a removable 3.7V lithium-ion battery. The robot is powered by strapping a jumper over the left-side pins. The two remaining pins on the right are for serial output, allowing to log information to the computer through the OHC. The OHC itself can be connected via a B-type USB cable, and used via a specific Graphical User Interface accessible at <https://github.com/acornejo/kilogui>.

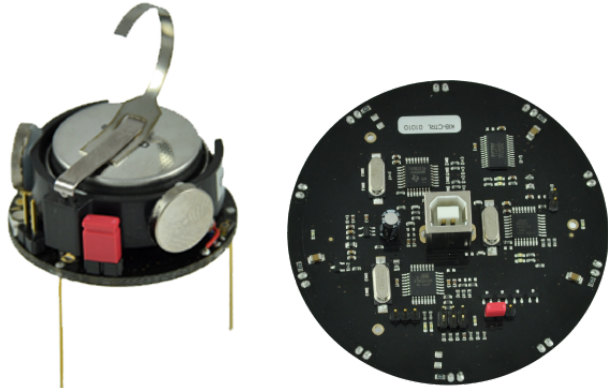


FIGURE 1

Left : A single Kilobot. Right : The Over-Head Controller

In order to move forward and rotate, the Kilobot makes use of its two lateral motors vibrating, generating movement in a slip-stick fashion. This principle, of converting the motor vibration to a forward force, has been studied and detailed in a Kilobot like robot in (2). In practice, due to this mode of locomotion, the individual Kilobot lacks consistency in its motion when no feedback loop is created to assess and rectify the trajectory on-the-go. Both position and angular noise are quite important relative to the desired movement, and a slight bending of the Kilobot's legs may change its behavior. In order to have a better understanding and control of the individual dynamics of a single Kilobot, we designed and 3D printed Exoskeletons replacing the default locomotion. Our version of "Augmented Kilobot" is detailed in 1.1.3. The bare Kilobot, according to (3), can move forward at approximately 1 cm/sec and rotate approximately at 45 degrees/sec.

The communication between Kilobots is made through the infrared LED transmitter and infrared photo-diode receiver, which are located in the bottom-center of the circuit board and are pointed directly downwards at the table. The emitters are wide-angle in such a way that the communication takes place by reflection on the support. (see ??) This way of transmitting information is quite dependent of the reflection of the support for the corresponding wavelength. By measuring the intensity of one upcoming signal, a KB can also calculate the distance to the emitter, which a sensing accuracy of ± 2 mm, and precision under 1 mm.

Regarding power consumption, each KB is shipped with a 3.7 V Li-Ion 160mAh battery, which can power the robot for 3-10 hours continuously or 3 months in sleep mode . Power is switched on and off by connecting or disconnecting the power jumper on the top-right side of the Kilobot. The battery can be charged by applying a continuous 6V current directly to the battery. If the battery is inserted in a KB it can also be charged through the accessible top part of the battery (GND) and the legs of the KB., If the battery is

inserted in a KB it can also be charged through the accessible top part of the battery (GND) and the legs of the KB.

The Kilobot is programmed using a dedicated Application Programming Interface (API) written in C, available at <https://github.com/acornejo/kilolib>. A full description of the API as well as code snippets can be found on the Kilobot User Manual (4) and on the Kilobots web page (5), the latter containing tutorials under the "Labs" tab.

The API works using two main functions, one called at the beginning of the program and the other looping indefinitely, in a same fashion as the Arduino API. Regarding the motor control, each motor is powered with Pulse-With-Modulation (PWM) signal, and the API allows to specify a desired intensity to run each motor on a scale of 0 to 255. In combination with the OHC GUI, it is possible to specify the value of special variables in each Kilobot (such as *kilo_turn_left* or *kilo_straight_right*) allowing to calibrate individually each robot and saving the motors intensities that suit the most a straight forward movement or a turn in both directions. It is important to notice that the relation between the motor intensity and speed is not trivial, we characterize briefly this relation in the case of our Augmented Kilobot in section 1.1.3.

1.1.2 Exoskeletons. In order to reduce positional and angular noise in the trajectory, augment responsiveness and ease detection via image, we decided to 3D print *exoskeletons* in which we encapsulate the bare Kilobots. Multiple exoskeletons were successively made which have shown that the morphology (meaning shape and structural features) of the robot deeply influence its dynamics. In particular, the so-called **and **exoskeletons both show remarkable behaviors when they are subject to an external force.****

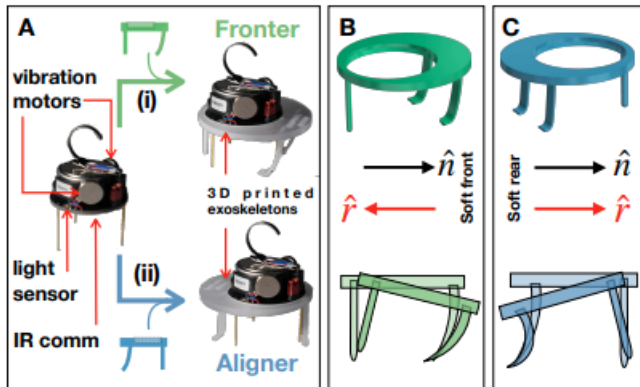


FIGURE 2
Pictures and 3D models of the frakter and aligner exoskeleton. Credit : Zion et al.2021 (6)

Both the aligner and the frakter shown in 2 are tripod based design, with a pair of flexible legs on one side and an opposing stiff leg, with both designs having a circular frame of diameter $d = 4.8\text{cm}$. These exoskeletons take inspiration from the self-propelled polar disks used in Deseigne et al. 2010 (7). When subjected to an external force such as gravity, the aligner polarity tends to align with the direction of said force, as the frakter tends to anti-align with the force. The dynamics of these exoskeleton is described further in section 2.1.

As we first tried to use the frakter exoskeleton as a baseline, we found out that it had some default that were hard to overcome. Mainly, their trajectory are still quite noisy, making it hard for the kilobots to have proper control of their trajectory. Secondly, the bendable legs are brittle, and the exoskeletons break easily.

In the end, we settled on a final exoskeleton for which the resulting combination of Kilobot + exoskeleton is what we call the **Augmented Kilobot**.

1.1.3 Augmented Kilobot.

We decided to 3D print exoskeletons attached to the Kilobots, the resulting combination of Kilobot + exoskeleton is what we call the Augmented Kilobot. This exoskeleton was made in the continuation of a series of older exoskeletons, which have shown that the morphology (meaning shape and structural features) of the robot deeply influence its dynamics. The transition from bare Kilobot to Augmented Kilobot serve multiple purposes, it greatly reduces positional and angular noise in the trajectory, augment responsiveness, ease detection via image and enables to easily change the outer shape of the robot, potentially influencing collisions dynamics.

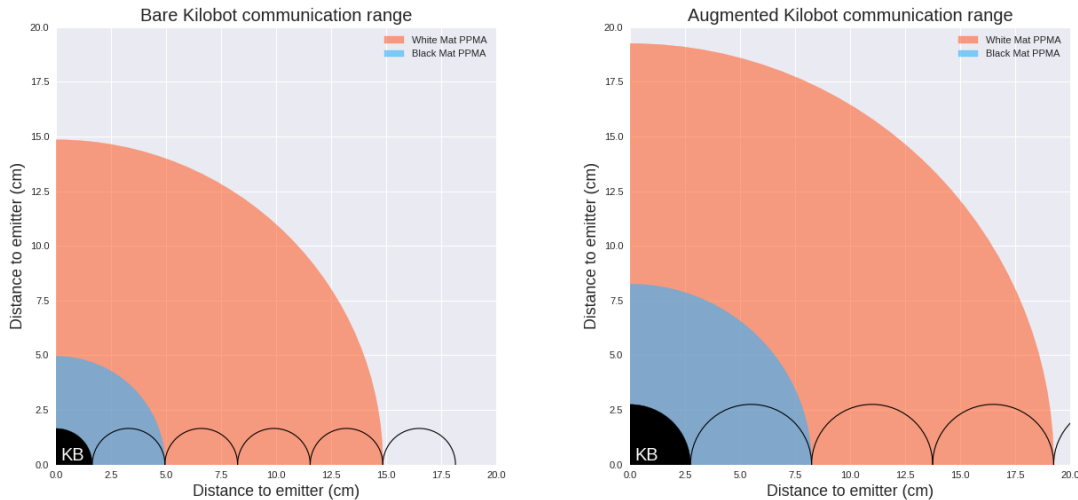
**FIGURE 3**

Corner view of a Kilobot inside its exoskeleton, namely an Augmented Kilobot.

Our Augmented Kilobot is 55mm wide and about 60 mm tall. The exoskeleton is 3D printed using a Stratasys Object360 printer, fully in Rigur RDG450 resin. It is made in two separate pieces, the core on which we glue the new legs, and the outer ring, defining the external shape. Both pieces are joined together by screwing the ring in a hollow part of the core. The top of the exoskeleton is colored black on the front side, and white on the back side, permitting a simple yet effective tracking using a camera mounted on top of our arena.

In contact with the support are shear-bent toothbrushes heads, replacing the Kilobot's legs. The multiplicity of the contact points and the flexibility of the nylon makes toothbrushes effective in combination with vibrating motors to produce a smooth forward movement, in a slip-stick fashion.

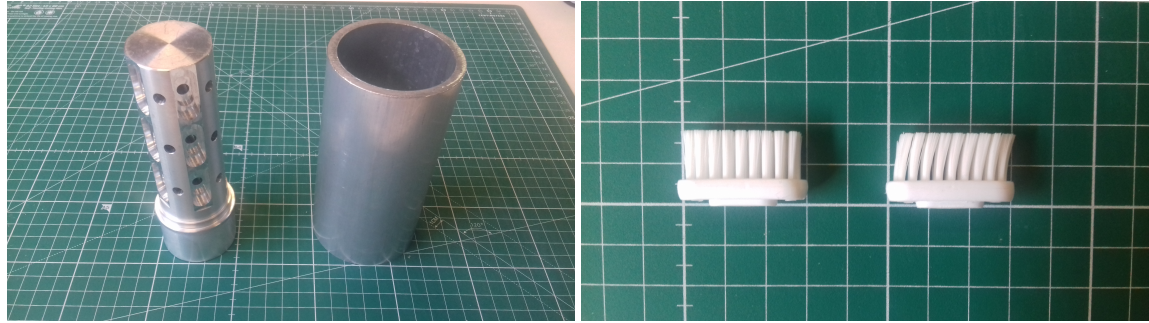
Since the Infrared Emitter-Receiver of the Kilobot is located underneath the PCB, this exoskeleton had to be high enough, such that the bottom plane on which the toothbrushes are glued interferes the least possible with the inter-Kilobot communication, while maintaining stability of the whole structure. We performed a series of simple communication tests in order to characterize roughly the difference between a bare Kilobot and a Kilobot with exoskeleton, on two different surfaces. Two Kilobots both with or without exoskeleton are placed at known distance from each other, on a given surface : either black mat PMMA or white mat PMMA. One is fixed and is sending 100 numbered packets, communication is considered valid if > 95 packets were correctly received. Distances used were in slices of 0.5 diameters. Results are shown in figure 4.

**FIGURE 4**

Approximate communication range for Kilobots over two different surfaces.

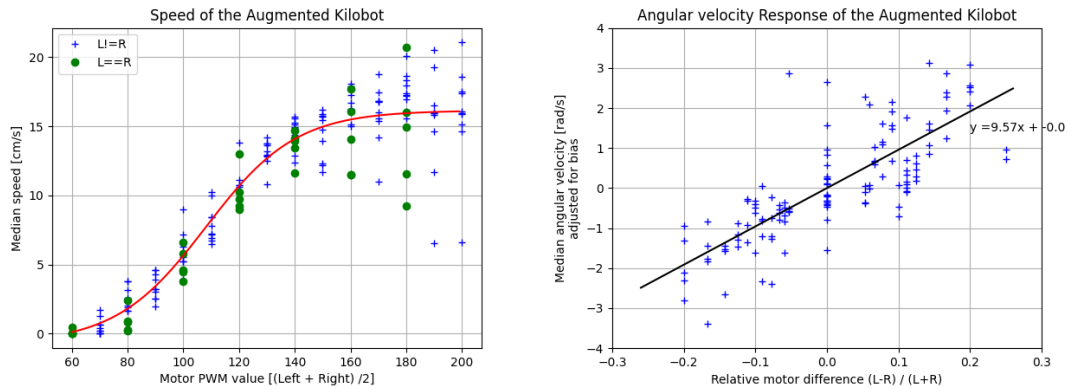
We see a difference between the white support and the black support, which can be explained *a priori* by a greater absorption in the wavelength used for communication by the black support.

Regarding the fabrication, the toothbrushes that we use are sold as rechargeable heads of plastic and perpendicularly stacked nylon 1010 filaments. This type of nylon has a relatively low glass transition temperature (around 41°C according to MS Wang · 1994 ?), allowing us to shear bend the filaments. The heads are placed in a tube designed for this purpose, applying compression and shear forces to the filaments. The tube is then heated to 60°C for 40 minutes, and is cooled down quickly under water.

**FIGURE 5**

Left : Aluminium device used to shear-bend the toothbrushes. **Right** : Before and after bending toothbrushes heads.

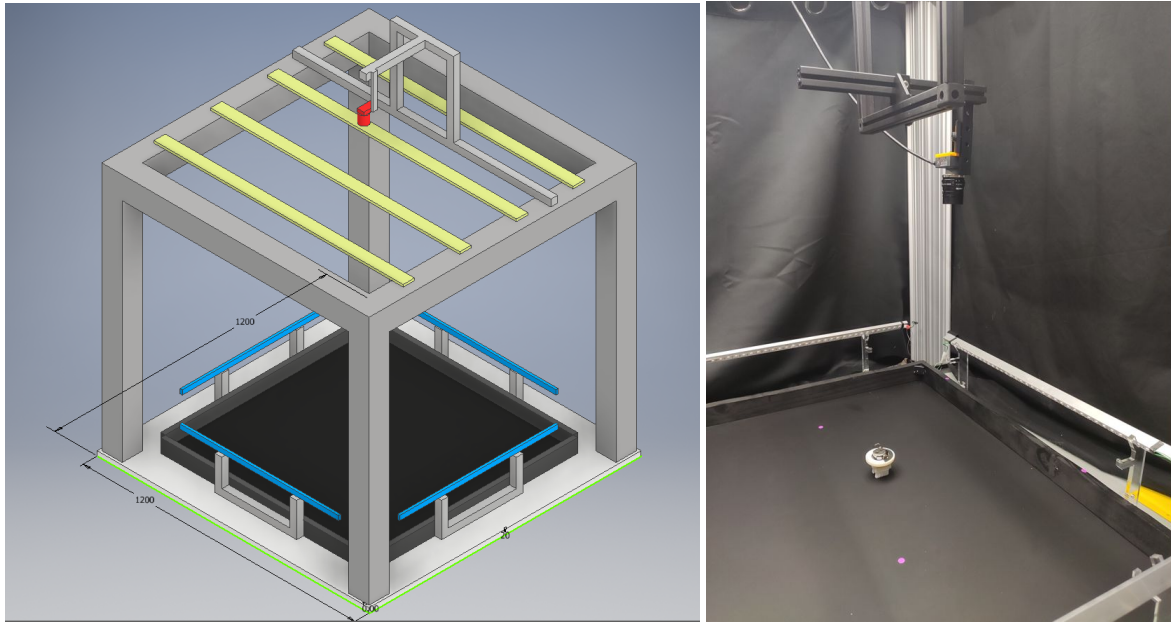
We performed a simple characterisation of the movement of individual robots in the arena, by analysing trajectories for different PWM values of the motors, for different exoskeletons. Each exoskeleton possess its bias, meaning that its angular velocity is not zero when having set its motors to the same value.

**FIGURE 6**

Left : Speed of the augmented Kilobot for different motor values, with fitting sigmoid in red. **Right** : Angular velocity of the augmented Kilobot for different motor values. In both experiments, 5 different exoskeletons where tested for 35 motor values.

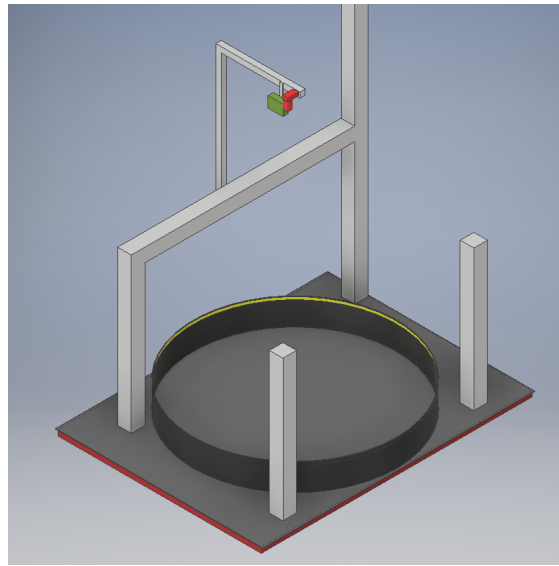
1.2 The Arena

1.2.1 Presentation of the setup. Augmented Kilobots move freely in a 90cm×90cm square, delimited by walls made out of strips of pine wood painted black. On top of the walls are placed strips of infrared LEDs of the same wavelength as the Kilobots connected to a micro-controller and acting as an arena-wide OHC. The surface of the arena is made of a 3mm thick black matte PMMA layer 3mm resting on top of a 2mm thick rubber sheet resting on an horizontally adjusted table. The surface and the walls are enclosed in a 1m×1m×1m cubic aluminium structure, holding on top of the surface a 12 MP camera equipped with a 12.6mm lens, centered and pointing downwards. The structure also holds 8 strips of cool white dimmable LEDs, as well as wide black sheets of fabric, separating the light of the setup from the one of the room.

**FIGURE 7**

Left : 3D Model of the arena. The parts in blue are the infrared LED strips used as custom OHC. The parts in yellow are the white dimmable LED strips providing light, the parts in red are the camera and lens. **Right** : Picture of the arena, with the camera moved to a narrow location.

The setup was updated in December 2021, in order to run a set of experiments in a circular arena of 1.5 meters in diameter. This new setup is fixed onto a thick slab of chipboard wood of 5x200x200cm on which beams are screwed in. The main beam structure is fixed along a bearing wall of the experimentation room, two beams are placed on the opposite side to hold the black fabric covering the whole arena. The circular wall is made of 20cm wide and 0.2mm thick aluminium sheet, on the inside of which the LEDs light strips have been set. The camera have been raised in order to film the entirety of the arena, and a video projector has been added next to the camera. Because they were not used in the set of experiment in this arena, the infrared LEDs have been removed in this setup.

**FIGURE 8**

3D Model of the 2nd arena. As in Figure 7, the LEDs strips are shown in yellow, the camera is in red, the projector in green.

1.2.2 Tracking of the Augmented Kilobots. In all of our experiments, the camera produces a binary file of known structure (see [PixelLINK Data Stream File Format](#)), in which we can access each frame by calculating its address in the binary file. The frames are saved as black and white with a 8-bit color depth, and we read directly the "Height × Width" bytes to a numpy array. We then perform a series of operations on the frame (*pipeline*) using OpenCV,

yielding at the end the position, direction and led state of each Augmented Kilobot. The details of this pipeline is given in figure 9.

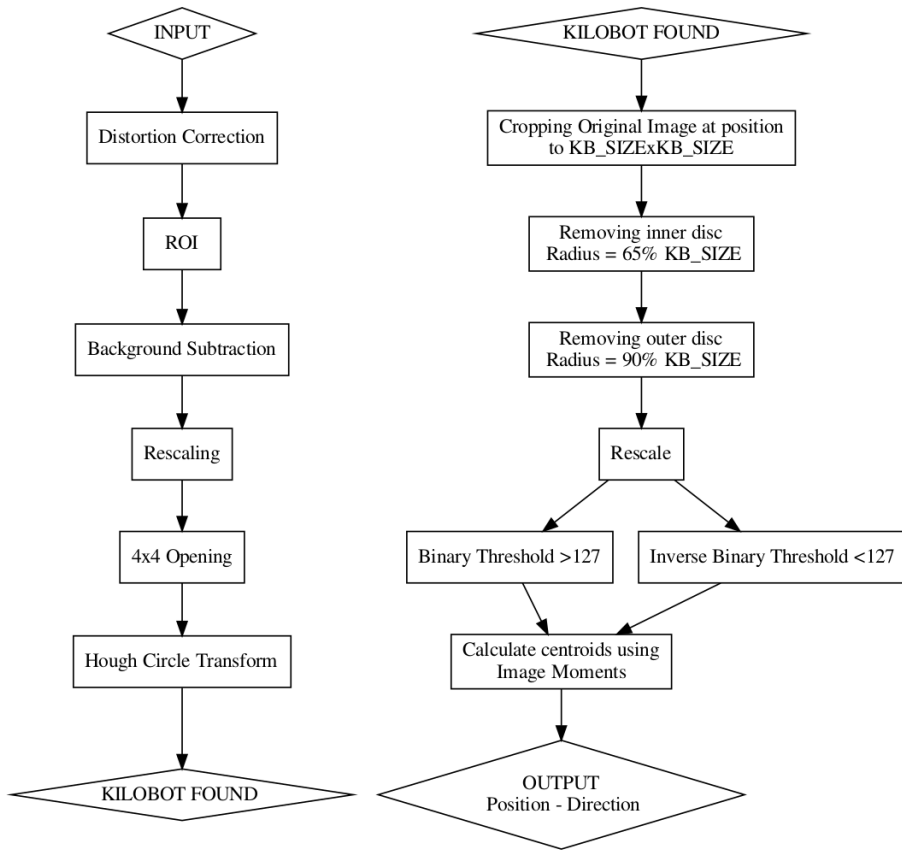


FIGURE 9
Augmented Kilobot Identification Pipeline.

All data extracted is exported as a .csv file, including frame index and mean pixel intensity of the picture as additional columns. Each time the tracking script is executed, a notice is generated indicating the time of extraction and compiling all the parameters used, in a way that the performed extraction is reproducible and any extraction error can be easily found and fixed.

2. Individual Dynamics of the Augmented Kilobot

2.1 State of the Art

The dynamical model we began to use in order to describe the motion of the augmented Kilobot is a relatively simple model, describing the motion of vibrated self-propelled polar disks (7) (8). This model couples the direction \mathbf{n} of each particle with their velocity \mathbf{v} in 2D, and assumes the dynamics on \mathbf{n} is over-damped. As \mathbf{v} is propelled forward via a force in the \mathbf{n} direction, \mathbf{n} turns continuously to \mathbf{v} via a torque proportional to the sin of the angle between \mathbf{n} and \mathbf{v} . A damping is added to \mathbf{v} such that the particle reaches a stationary speed. We obtain the following set of equations :

$$m\dot{\mathbf{v}} = F_0\mathbf{n} - \gamma\mathbf{v} + \Sigma\tilde{\mathbf{f}} \quad (1)$$

$$\Omega\dot{\mathbf{n}} = \zeta(\mathbf{n} \times \mathbf{v}) \times \mathbf{n} \quad (2)$$

Each coefficient is defined positive. Let $v_0 = F_0/\gamma$ denotes the final speed of the isolated particle. We choose the mass m of the particles, their diameter d , and d/v_0 , as units of mass, length and time. The above arguments are cast into the following dimensionless equations :

$$\tau_v\dot{\mathbf{v}} = \mathbf{n} - \mathbf{v} + \Sigma\tilde{\mathbf{f}} \quad (3)$$

$$\tau_n\dot{\mathbf{n}} = (\mathbf{n} \times \mathbf{v}) \times \mathbf{n} \quad (4)$$

with $\tau_v = \frac{mv_0}{\gamma d}$, $\tau_n = \frac{\Omega}{d\zeta}$ and $\Sigma\tilde{\mathbf{f}} = \frac{\Sigma\tilde{\mathbf{f}}}{\gamma v_0}$.

This model is simple yet powerful enough to describe the dynamics of the vibrated polar disks, as well as the dynamics of Hexbugs (9). However, we found out that in specific situations, the model did not match the dynamics of our augmented Kilobots. The observed trajectories diverges particularly in two situations. When put on an Inclined Plane, thus imposing a constant force along a given axis, an augmented Kilobot turns into *or opposed to* the direction of the applied force ! Also he doesn't reach it or overshoots it asymptotically, indicating the presence of a bias in its motion. Also, when hitting a Wall, the dynamics give rise to oscillations including a combination of rolling and sliding.

2.2 The Augmented Kilobot

In the model describe in section 2.1, the dynamics on $\dot{\mathbf{n}}$ is supposed over-damped. We began to expand the model by considering the dynamics on $\dot{\mathbf{n}}$ no longer over-damped, as well as adding a constant torque, the bias b , which although small compared to the velocity-induced torque, cannot be neglected, as the *Inclined Plane* experiment shows. Writing $\mathbf{n} = \begin{pmatrix} \cos \theta \\ \sin \theta \end{pmatrix}$, in an arbitrary reference frame $(\mathbf{e}_x, \mathbf{e}_y)$, we obtain the following equations for the dynamics :

$$\begin{cases} mv_x = F_0 \cos \theta - \gamma v_x + \Sigma\tilde{\mathbf{f}}_x \\ mv_y = F_0 \sin \theta - \gamma v_y + \Sigma\tilde{\mathbf{f}}_y \\ \dot{\theta} = \omega \\ I\dot{\omega} = \zeta(\cos \theta v_y - \sin \theta v_x) - \Omega\omega + \tilde{b} \end{cases} \quad (5)$$

where I is the angular moment of inertia and \tilde{b} is the angular bias. Here, ζ can be positive or negative, the corresponding dynamics being said to be the one of an *, respectively a *fronter*. Let $\epsilon = \text{sign}(\zeta)$, which value is +1 for an aligner, -1 for a fronter. Again, we perform nondimensionalization of the equations with the characteristic speed $v_0 = F_0/\gamma$, mass m and length d_0 , yielding*

$$\begin{cases} \tau_v\dot{v}_x = \cos \theta - v_x + \Sigma\tilde{\mathbf{f}}_x \\ \tau_v\dot{v}_y = \sin \theta - v_y + \Sigma\tilde{\mathbf{f}}_y \\ \dot{\theta} = \omega \\ J\dot{\omega} = \epsilon(\cos \theta v_y - \sin \theta v_x) - \tau_n\omega + b \end{cases} \quad (6)$$

with $\tau_v = \frac{mv_0}{\gamma d}$, $\Sigma\tilde{\mathbf{f}} = \frac{\Sigma\tilde{\mathbf{f}}}{\gamma v_0}$, $J = \frac{Iv_0}{|\zeta|d^2}$, $\tau_n = \frac{\Omega}{|\zeta|d}$ and $b = \frac{\tilde{b}}{|\zeta|v_0}$.

2.3 The free particle : $\Sigma f = 0$

In the absence of external force (or for a central force) the isotropy of space suggest that only the difference of orientation between \mathbf{n} and \mathbf{v} matters. We thus introduce $\mathbf{v} = v \begin{pmatrix} \cos \phi \\ \sin \phi \end{pmatrix}$ and $\alpha = \theta - \phi$ to obtain the free particle equations :

$$\begin{cases} \tau_v \dot{v} = \cos \alpha - v \\ \tau_v \dot{\phi} = \frac{1}{v} \sin \alpha \\ \dot{\alpha} = \omega - \frac{1}{\tau_v v} \sin \alpha \\ J \dot{\omega} = -\epsilon v \sin \alpha - \tau_n \omega + b \end{cases} \quad (7)$$

The first two equations respectively describe the translational and orientational motion of a frame tangent to the trajectory of the particles. In agreement with the isotropy of space, the variable ϕ does not enter in the equations, except for the second one describing its dynamics, once v and α are known.

In the following we shall look for simple "steady" solutions, namely straight line or circular motion, that is solutions for which α , v , and ω are constant.

2.3.1 Case $b = 0$, no bias. This subcase does not need to be separated from the general case, but it provides a nice illustration of the difference between the aligners and the frontiers in a simplified setting.

$$\begin{cases} \tau_v \dot{v} = \cos \alpha - v \\ \dot{\alpha} = \omega - \frac{1}{\tau_v v} \sin \alpha \\ J \dot{\omega} = -\epsilon v \sin \alpha - \tau_n \omega \end{cases} \quad (8)$$

Considering the fixed points $\dot{\alpha} = \dot{v} = \dot{\omega} = 0$, the equations for strongly simplify into :

$$\begin{cases} v^* = \cos \alpha^* \alpha^* = -\frac{1}{\tau_n} \epsilon v \sin \alpha^* - \frac{1}{\tau_v v} \sin \alpha^* \\ \omega^* = -\frac{1}{\tau_n} \epsilon v \sin \alpha^* \end{cases} \quad (9)$$

With the following solution for v and α :

$$\begin{cases} v^* = \cos \alpha^* \quad \text{with} \quad v^* > 0 \\ \sin \alpha^* = 0 \quad \text{or} \quad \cos^2 \alpha^* = -\epsilon \frac{\tau_n}{\tau_v} \end{cases} \quad (10)$$

The stability of the solutions are given by the sign of the real part of the eigenvalues of the matrix :

$$\begin{pmatrix} \dot{v} \\ \dot{\alpha} \\ \dot{\omega} \end{pmatrix} = \begin{pmatrix} -\frac{1}{\tau_v} & -\frac{\sin \alpha^*}{\tau_v} & 0 \\ \sin(\alpha^*) \left(\frac{-\frac{1}{\tau_v}}{\tau_v \cos^2 \alpha^*} - \epsilon \frac{1}{\tau_n} \right) & -\epsilon \frac{1}{\tau_n} \cos^2 \alpha^* - \frac{1}{\tau_v} & 0 \\ ??? & ??? & -\frac{\tau_n}{J} \end{pmatrix} \begin{pmatrix} dv \\ d\alpha \\ d\omega \end{pmatrix} \quad (11)$$

the characteristic polynomial of which is :

$$\left(-\frac{\tau_n}{J} - \lambda \right) \left[\lambda^2 + \lambda \left(\frac{2}{\tau_v} + \epsilon \frac{1}{\tau_n} \cos^2 \alpha^* \right) + \left(\epsilon \frac{1}{\tau_v \tau_n} \cos^2 \alpha^* + \frac{1}{\tau_v^2} + \frac{1}{\tau_v^2} \tan^2 \alpha^* - \epsilon \sin^2 \alpha^* \frac{1}{\tau_v \tau_n} \right) \right] \quad (12)$$

Aligner, $\epsilon = 1$. The only fixed point is $\alpha^* = 0, v^* = 1$; hence $\dot{\phi} = 0$. The velocity is aligned with the polarity and the particle performs a straight motion. This straight trajectory is always linearly stable.

Frontier, $\epsilon = -1$. When $\tau_v / \tau_n > 1$, two additional solutions emerge : $\alpha^* = \pm \arccos \left(\sqrt{\frac{\tau_n}{\tau_v}} \right)$, $v^* = \sqrt{\frac{\tau_n}{\tau_v}}$. Here $\dot{\phi} = \frac{1}{\sqrt{\tau_n \tau_v}} \sin \alpha^*$ is non zero. The particle orbits on a circle of radius $R^* = v^*/\dot{\phi} = \frac{1}{\tau_v \sin \alpha^*}$. The straight trajectory becomes unstable when $\frac{\tau_n}{\tau_v} > 1$, and is replaced by the circular motion which is linearly stable. The bifurcation diagram is given on Figure 10.

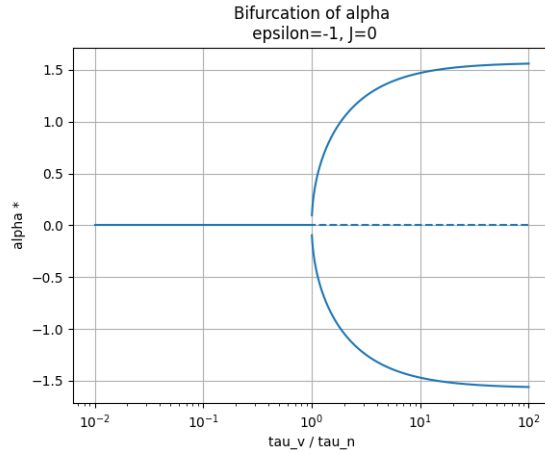


FIGURE 10
Bifurcation diagram, for a frontier without bias; $b=0$.

2.3.2 General case. Looking for solutions with $\dot{v} = \dot{\alpha} = \dot{\omega} = 0$, we end up with the following equations :

$$\begin{cases} v^* = \cos \alpha^* \\ \omega^* = \frac{1}{\tau_v} \tan \alpha^* \\ \frac{\tau_n}{\tau_v} \tan \alpha^* = -\epsilon \cos \alpha^* \sin \alpha^* + b \end{cases} \quad (13)$$

Denoting $t = \tan(\alpha^*)$ we find solutions as root of a polynomial :

$$\frac{\tau_n}{\tau_v} t^3 - bt^2 + t\left(\epsilon + \frac{\tau_n}{\tau_v}\right) - b = 0 \quad (14)$$

and their linear stability is given by the sign of the real part of the eigenvalues of the following matrix :

$$\begin{pmatrix} \dot{v} \\ \dot{\alpha} \\ \dot{\omega} \end{pmatrix} = \begin{pmatrix} -\frac{1}{\tau_v} & -\frac{\sin \alpha^*}{\tau_v} & 0 \\ \frac{\sin \alpha^*}{\tau_v \cos^2 \alpha^*} & -\frac{1}{\tau_v} & 1 \\ -\epsilon \frac{\sin \alpha^*}{J} & -\epsilon \frac{\cos^2 \alpha^*}{J} & -\frac{\tau_n}{J} \end{pmatrix} \begin{pmatrix} dv \\ d\alpha \\ d\omega \end{pmatrix} \quad (15)$$

the characteristic polynomial of which reads

$$-\lambda^3 - \lambda^2 \left[\frac{\tau_n}{J} + \frac{2}{\tau_v} \right] - \lambda \left[\frac{1}{\tau_v^2} + \frac{2\tau_n}{\tau_v J} + \epsilon \frac{\cos^2 \alpha^*}{J} + \frac{\tan^2 \alpha^*}{\tau_v^2} \right] - \left[\frac{\tau_n}{\tau_v^2 J} + \epsilon \frac{\cos(2\alpha^*)}{\tau_v J} + \frac{\tau_n \tan^2 \alpha^*}{\tau_v^2 J} \right] \quad (16)$$

Aligner, $\epsilon = 1$

In the simple case $b = 0$, we found $\alpha^* = 0$, corresponding to the straight line motion, is the only solution. When $b \neq 0$, we first find that the linear motion is replaced by a slowly rotating circular motion, $\omega^* = \frac{\tan \alpha^*}{\tau_v}$, the radius of which $R^* = \frac{1}{\tau_v \sin \alpha^*}$ decreases from infinity when the bias grows from zero. Second, we find two other branches of circular motion solutions, only one of which is linearly stable. It has much smaller radius of gyration and must faster angular velocity.

- For $b \lesssim 0.5$, the two circular motion are *disconnected* and the fast one disappear in a saddle node bifurcation when τ_v/τ_n becomes smaller than some critical value, which decreases when b increases.
- For $b \gtrsim 0.5$, the two circular solution connects in an imperfect bifurcation.

The corresponding bifurcation diagrams are shown in Figure 11.

Frontier, $\epsilon = -1$

In the simple case $b = 0$, we found that the straight line trajectory $\alpha^* = 0$, bifurcates super-critically into a circular trajectory $\alpha^* = \pm \arccos \left(\sqrt{\frac{\tau_n}{\tau_v}} \right)$, when $\tau_v > \tau_n$. In the presence of a bias, the bifurcation becomes

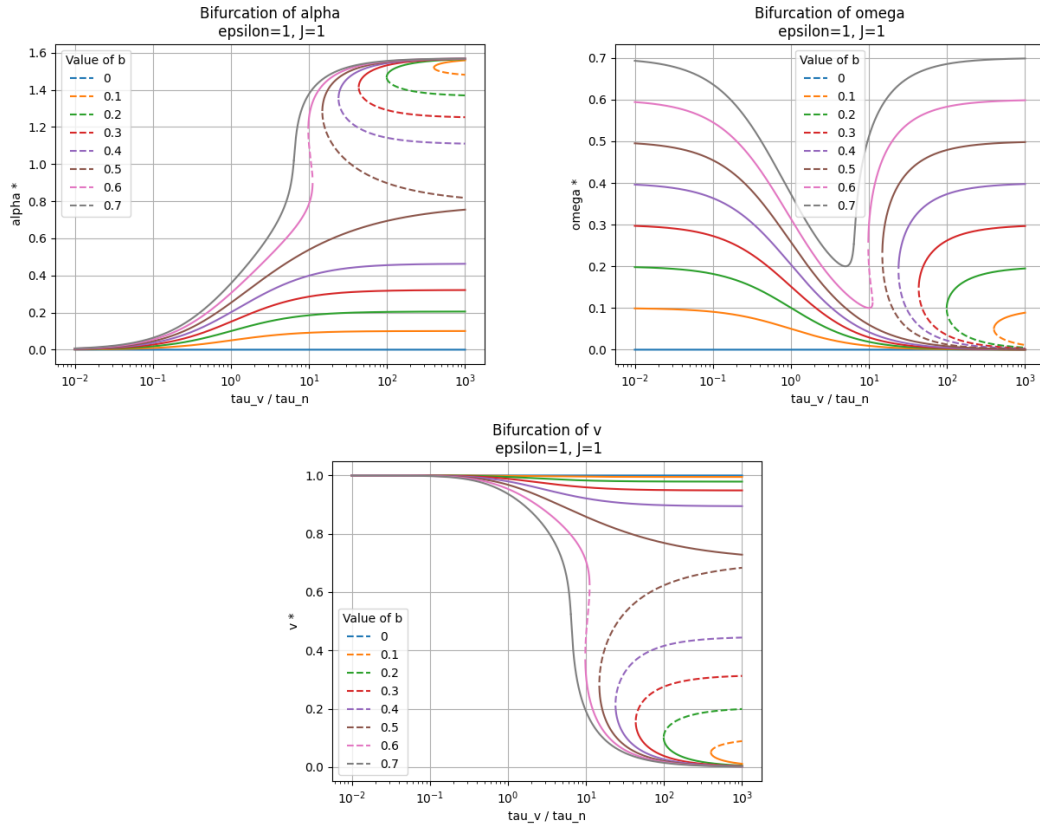


FIGURE 11
Aligner bifurcation diagrams.

imperfect. One of the bifurcated branch connects continuously to the straight trajectory solution. The other one connects in a saddle node bifurcation to the linearly unstable straight trajectory : the exact analogue of the Ising bifurcation in the presence of an external field. Note that ω^* is maximal close to the bifurcation. The bifurcation diagrams that we obtain are shown in Figure 12.

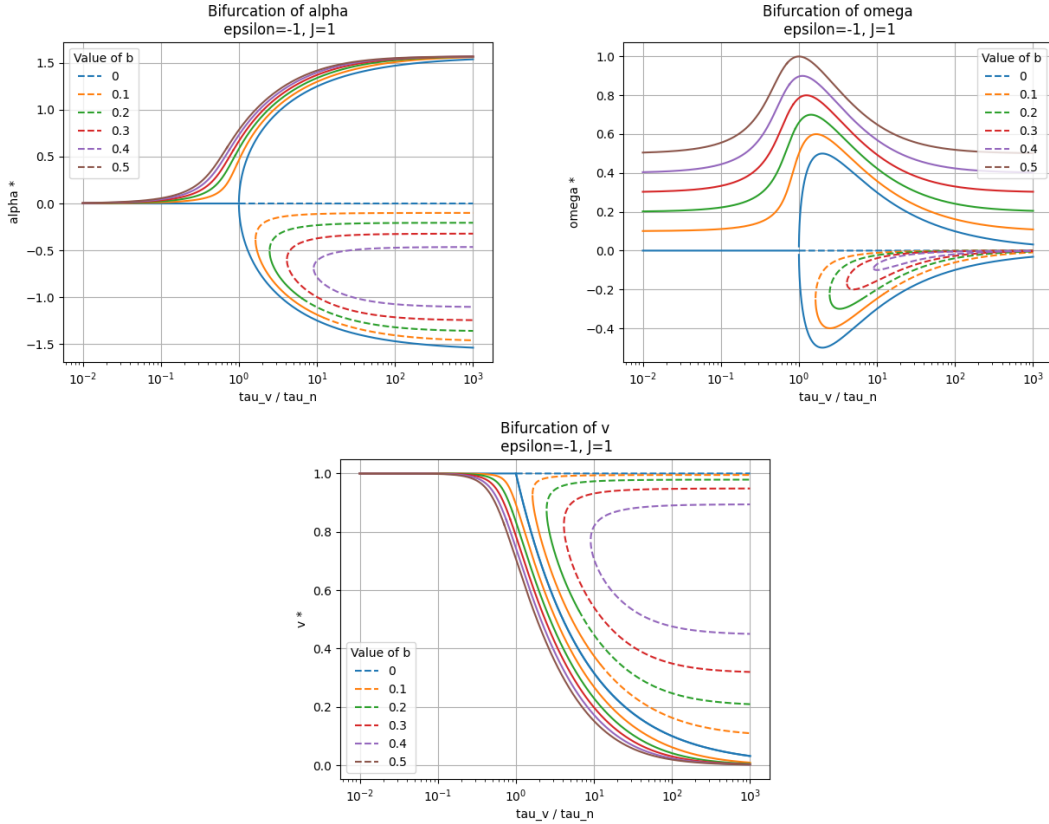


FIGURE 12
Frontier bifurcation diagrams

2.4 Inclined Plane : $\Sigma f \neq 0$

We now consider the case corresponding to the incline plane experiment, where the particle experiences a constant external body force, say in the direction \mathbf{e}_x . The experiment consists of a rigid plane inclined a few degrees along the \mathbf{e}_x axis. For different inclinations, we obtain an effective gravity uniformly affecting the space in which the Kilobot moves. Let α_h denote the angle to the horizontal, the dimensionless force applied is given by :

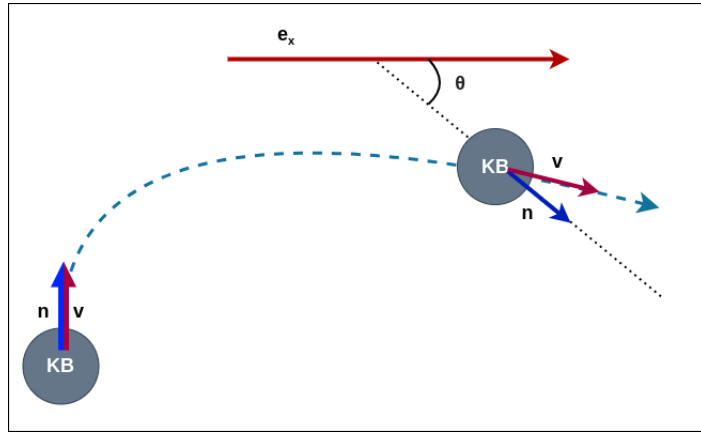
$$\mathbf{f}_{plane} = \frac{m\tilde{g} \sin(\alpha_h)}{\gamma v_0} \mathbf{e}_x = g\mathbf{e}_x$$

The isotropy of space being broken, we come back to the Cartesian formulation :

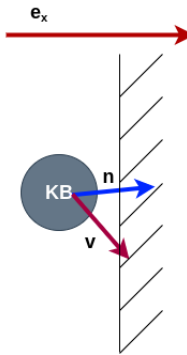
$$\begin{cases} \tau_v \dot{v}_x = \cos \theta - v_x + g \\ \tau_v \dot{v}_y = \sin \theta - v_y \\ \dot{\theta} = \omega \\ J \ddot{\omega} = \epsilon(\cos \theta v_y - \sin \theta v_x) - \tau_n \omega + b \end{cases} \quad (17)$$

As observed in the experiments, the circular solutions turn into more complex cycloids, for which there is no chance to capture the analytical expression. We therefore concentrate on the straight trajectories for which $\dot{\theta} = \dot{v}_x = \dot{v}_y = 0$ and find

$$\begin{cases} v_x^* = g + \sqrt{1 - \frac{b^2}{g^2}} \\ v_y^* = \epsilon \frac{b}{g} \\ \sin \theta^* = \epsilon \frac{b}{g} \end{cases} \quad (18)$$

**FIGURE 13**

Sketch of the inclined plane experiment. The velocity always has a final angle to e_x smaller than θ .

**FIGURE 14**

Sketch of the wall experiment.

Hence the straight trajectory exists only when the bias is not too strong, namely $b < g$; the trajectory makes an angle θ with the applied force.

The linear stability is given by the sign of the real part of the eigenvalues of the matrix :

$$\begin{pmatrix} \dot{v}_x \\ \dot{v}_y \\ \dot{\theta} \\ \dot{\omega} \end{pmatrix} = \begin{pmatrix} -\frac{1}{\tau_v} & 0 & -\epsilon \frac{b}{g\tau_v} & 0 \\ 0 & -\frac{1}{\tau_v} & \frac{\sqrt{1-\frac{b^2}{g^2}}}{\tau_v} & 0 \\ 0 & 0 & 0 & 1 \\ -\frac{b}{gJ} \epsilon \frac{\sqrt{1-\frac{b^2}{g^2}}}{J} & -\epsilon \frac{\sqrt{g^2-b^2}+1}{J} & -\frac{\tau_n}{J} \end{pmatrix} \begin{pmatrix} dv_x \\ dv_y \\ d\theta \\ d\omega \end{pmatrix} \quad (19)$$

the characteristic polynomial of which reads :

$$(-\lambda - \frac{1}{\tau_v}) \left(-\frac{\lambda \epsilon (\sqrt{g^2 - b^2} + 1)}{J} - \frac{\epsilon (\sqrt{g^2 - b^2} + 1)}{\tau_v J} + \frac{\epsilon b^2}{g^2 J} \right) + \frac{\epsilon (1 - \frac{b^2}{g^2})(-\lambda - \frac{1}{\tau_v})}{\tau_v J} - (\lambda^3 + \frac{\lambda}{\tau_v^2} + \frac{2\lambda^2}{\tau_v})(-\frac{\tau_n}{J} - \lambda) \quad (20)$$

2.5 Dynamics against straight walls

When the augmented Kilobot is pushing against a static wall, both its velocity in the direction parallel to the wall and the angle of its polarity with the wall start to oscillate (see Figure 14, [GIF example](#)) with a growing amplitude. The maximum amplitude of these oscillations increases with the an increase of initial speed. If the initial speed is too small, the Kilobot may stay against the wall for an undefined period of time, and if it is too big the Kilobot leaves the wall after a few periods.

Simulating the previous equations against a wall modeled as a stiff interaction potential, we find that inertia on $\dot{\theta}$ and v is not sufficient to generate any form of oscillating behavior. The description of the interaction with

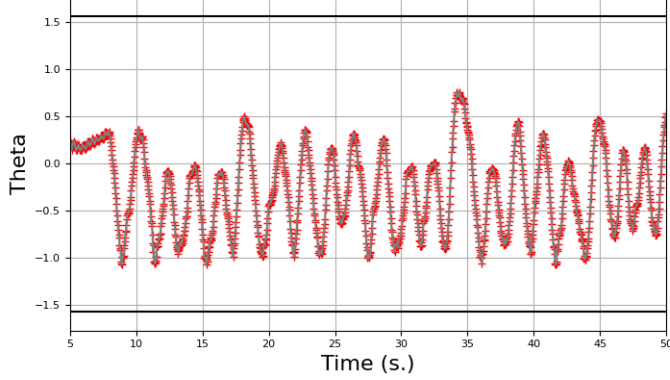


FIGURE 15
Orientation of the augmented Kilobot pushing against a wall, initial speed $\approx 7\text{cm}.s^{-1}$.

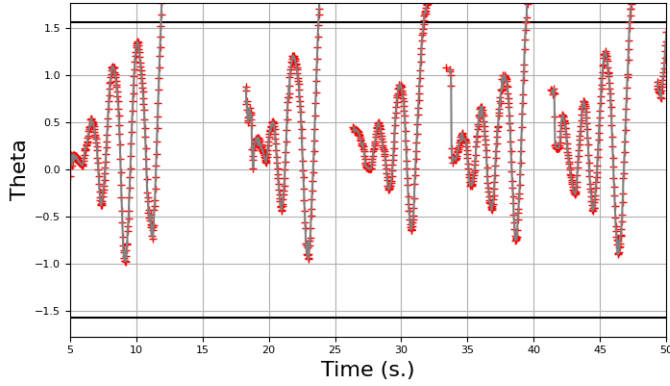


FIGURE 16
Orientation of the augmented Kilobot pushing against a wall, initial speed $\approx 20\text{cm}.s^{-1}$.

the wall must include a component parallel to the wall. The most general kinematics of a rolling disk in contact with a plane is that of rolling with sliding, which we now implement in the model.

We consider an infinitely long wall along the \mathbf{e}_y direction, located at $x = 0$, and described by some repulsive potential V_w , typically the WCA potential, of width $\sigma = \frac{d}{2}2^{-\frac{1}{6}}$ and depth $\epsilon = 1$:

$$V_{wall} = \begin{cases} (\frac{d}{2x})^{12} - 2(\frac{d}{2x})^6 + 1 & x > -\frac{d}{2} \\ 0 & x \leq -\frac{d}{2} \end{cases} \quad (21)$$

The wall is then modeled as a repulsion force, a damping force and a torque as follows which become non zero when $x > -d/2$.

$$\mathbf{f}_{\perp} = -\frac{\partial V_w}{\partial x} \mathbf{e}_x \quad (22)$$

$$\mathbf{f}_{\parallel} = -\mu u \mathbf{e}_y \quad (23)$$

$$\Gamma_w = -\mu u \frac{d}{2} \quad (24)$$

where $u = v_y + \frac{d}{2}\dot{\theta}$ is the sliding speed along the wall, μ is the wall friction coefficient. Describing the wall using both a continuous potential and a contact law requires some precision. When simulating the full 2d model, we will introduce a smooth filter on \mathbf{f}_{\parallel} and Γ_w to describe the continuous formation of the contact, as described by the continuous potential. For now, we analyze the model theoretically, assume permanent contact ($x = -d/2; v_x = 0$)

and analyze the reduced set of equations for the position along \mathbf{e}_y and the orientation of the Kilobot :

$$\begin{cases} mv_y = F_0 n_y - \gamma v_y - \mu u \\ I\ddot{\theta} = \zeta \cos \theta v_y - \Omega \dot{\theta} + \tilde{b} - \mu u \frac{d}{2} \end{cases} \quad (25)$$

Once again, considering v_0 the final speed of the isolated particle, we re-scale mass, length and time with m , d and d/v_0 and replacing u with $v_y + \frac{1}{2}\dot{\theta}$, the final equations modeling a permanent contact with the wall read :

$$\begin{cases} \tau_v v_y = \sin \theta - (1 + \lambda)v_y - \frac{1}{2}\lambda \dot{\theta} \\ J\ddot{\theta} = (\cos \theta - \tau_r)v_y - (\tau_n + \frac{1}{2}\tau_r)\dot{\theta} + b \end{cases} \quad (26)$$

with $\tau_v = \frac{mv_0}{\gamma d}$, $\lambda = \frac{\mu}{\gamma}$, $J = \frac{Iv_0}{|\zeta|d^2}$, $\tau_n = \frac{\Omega}{|\zeta|d}$, $\tau_r = \frac{\mu d}{2\zeta}$ and $b = \frac{\tilde{b}}{|\zeta|v_0}$.

In the following, we assume $b = 0$ as a mean of simplification. It is clear that the bias will make the oscillation asymmetric, but at least when the natural motion of the Kilobot is the straight trajectory, we don't expect the bias to strongly alter the analysis.

In the absence of angular inertia $J = 0$

When, $J = 0$, the simplified 1d-model equations recast in two first order ODE for θ and v_y :

$$\begin{cases} \tau_v v_y = \sin \theta - (1 + \lambda)v_y - \frac{1}{2}\lambda \dot{\theta} \\ (\tau_n + \frac{1}{2}\tau_r)\dot{\theta} = (\cos \theta - \tau_r)v_y \end{cases} \quad (27)$$

These equations have two fixed points : a static fixed point $(v_y^0, \theta^0) = (0, 0)$, which exists for all values of the parameters, and a sliding solution $(v_y^*, \theta^*) = (\frac{\sqrt{1-\tau_r^2}}{1+\lambda}, \arccos \tau_r)$ when $|\tau_r| \leq 1$.

We could also not find any oscillating solutions, when exploring the equations numerically. It is likely that angular inertia is necessary to generate any form of oscillation, as seen in Figure 17

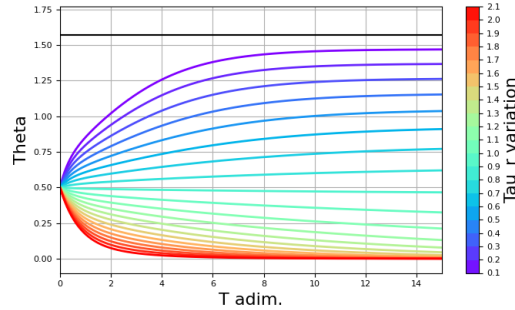


FIGURE 17

Evolution of θ over time for different values of τ_r , in the absence of angular inertia. $\tau_v = \tau_n = \lambda = 1$

Including angular inertia $J \neq 0$

2.6 Parameter exploration

Assuming $J \neq 0$, we have a space of 5 independent parameters to work with. Equation 26 can be linearized close to the fixed point $v_y^* = \theta^* = 0$:

$$\begin{pmatrix} \dot{\theta} \\ \ddot{\theta} \\ v_y \end{pmatrix} = \begin{pmatrix} 0 & 1 & 0 \\ 0 & -\frac{\tau_n + \frac{1}{2}\tau_r}{J} & \frac{1-\tau_r}{J} \\ \frac{1}{\tau_v} & -\frac{\lambda}{2\tau_v} & -\frac{1+\lambda}{\tau_v} v_y \end{pmatrix} \begin{pmatrix} \theta \\ \dot{\theta} \\ v_y \end{pmatrix} \quad (28)$$

The eigenvalues of the matrix gives us insights on the existence of oscillations. For diverse sets of parameters, complex eigenvalues with positive real part can be found. Unfortunately, due to the high number of parameters, the analytical solution can hardly be apprehended *as is*, because of the complexity of its expression. We therefore resort to numerical exploration of the parameters.

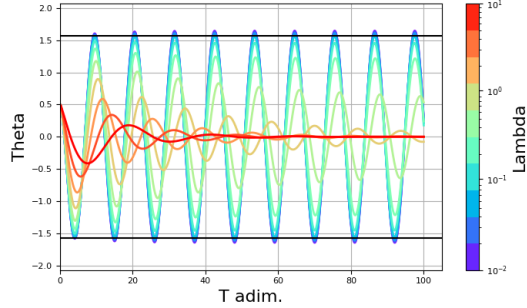


FIGURE 18

Singular set of parameters for which stable oscillations appears.

2.7 Extracting parameters from data

- b is obtained on the inclined plane with different angles, via the relation $b = g \sin \theta^*$
- τ_v can be obtained by measuring the radius of a trajectory on an horizontal plane, $R^* = \frac{1}{\tau_v \sin \alpha^*}$
- τ_n is recovered via the equation 14, yielding $\tau_n = \tau_v \frac{b+bt^2-t}{t^3+t}$ with $t = \tan \alpha^*$

3. Conclusion and perspectives

The first half of the PhD was mainly concerned with setting up the experimental setup, as well as the individual characterization of the kilobots and exoskeletons. The experimental setup was modified in December 2021, the work in progress since then concerns experiments using the exoskeletons presented in Figure 2. The aim is to implement the HIT distributed evolution algorithm (10) to accomplish a phototaxis task with 64 robots, according to the article (6). The rest of the PhD will focus on experiments using toothbrush exoskeletons (Augmented Kilobots) for phototaxis or box-pushing tasks. We will also compare the dynamical model against wall applied to robot-robot collisions to real collisions. Finally, it will be possible to use the extracted dynamic parameters to perform simulation experiments involving a larger number of robots.

References

- [1] Michael Rubenstein, Alejandro Cornejo, and Radhika Nagpal. Programmable self-assembly in a thousand-robot swarm. *Science*, 345(6198) :795–799, 2014.
- [2] Panagiotis Vartholomeos and Evangelos Papadopoulos. Analysis, design and control of a planar micro-robot driven by two centripetal-force actuators. In *Proceedings 2006 IEEE International Conference on Robotics and Automation, 2006. ICRA 2006.*, pages 649–654. IEEE, 2006.
- [3] Michael Rubenstein, Christian Ahler, and Radhika Nagpal. Kilobot : A low cost scalable robot system for collective behaviors. In *2012 IEEE international conference on robotics and automation*, pages 3293–3298. IEEE, 2012.
- [4] K-Team. Kilobot user manual version 2.0.
http://ftp.k-team.com/kilobot/user_manual/Kilobot_UserManual.pdf, 2016. [Online ; accessed 09-September-2021].
- [5] K-Team. Kilobotics website. <https://kilobotics.com/>, 2020. [Online ; accessed 09-September-2021].
- [6] Matan Yah Ben Zion, Nicolas Bredeche, and Olivier Dauchot. Distributed on-line reinforcement learning in a swarm of sterically interacting robots. *arXiv preprint arXiv:2111.06953*, 2021.
- [7] Julien Deseigne, Olivier Dauchot, and Hugues Chaté. Collective motion of vibrated polar disks. *Physical review letters*, 105(9) :098001, 2010.
- [8] Khanh-Dang Nguyen Thu Lam, Michael Schindler, and Olivier Dauchot. Self-propelled hard disks : implicit alignment and transition to collective motion. *New Journal of Physics*, 17(11) :113056, 2015.
- [9] P. Baconnier, D. Shohat, C. Hernandèz, C. Coulais, V. Démery, G. Düring, and O. Dauchot. Selective and collective actuation in active solids, 2021.
- [10] Nicolas Fontbonne, Olivier Dauchot, and Nicolas Bredeche. Distributed on-line learning in swarm robotics with limited communication bandwidth. In *2020 IEEE Congress on Evolutionary Computation (CEC)*, pages 1–8. IEEE, 2020.

